Gravitational lensing of extended high-redshift sources by dark matter haloes

F. Perrotta,[1,2]★ C. Baccigalupi,[2]★ M. Bartelmann,[3]★ G. De Zotti[1]★ and G. L. Granato[1]★

[1]*Oss. Astr. Padova, Vicolo dell'Osservatorio 5, I-35122 Padova, Italy*
[2]*SISSA/ISAS, Astrophysics Sector, Via Beirut, 4, I-34014 Trieste, Italy*
[3]*Max-Planck Institut für Astrophysik, PO Box 1317, D−85741 Garching, Germany*

ABSTRACT

High-redshift galaxies and quasi-stellar objects (QSOs) are most likely to be strongly lensed by intervening haloes between the source and the observer. In addition, a large fraction of lensed sources is expected to be seen in the submillimetre region, as a result of the enhanced magnification bias on the steep intrinsic number counts. We extend in three directions Blain's earlier study of this effect.

First, we use a modification of the Press−Schechter mass function and detailed lens models to compute the magnification probability distribution. We compare the magnification cross-sections of populations of singular isothermal spheres and Navarro, Frenk & White (NFW) haloes and find that they are very similar, in contrast to the image-splitting statistics which were recently investigated in other studies. The distinction between the two types of density profile is therefore irrelevant for our purposes.

Secondly, we discuss quantitatively the maximum magnification, μ_{max}, that can be achieved for extended sources (galaxies) with realistic luminosity profiles, taking into account the possible ellipticity of the lensing potential. We find that μ_{max} plausibly falls into the range 10–30 for sources of 1–$10\,h^{-1}$ kpc effective radius at redshifts within 1–4.

Thirdly, we apply our model for the lensing magnification to a class of sources following the luminosity evolution typical for a unified scheme of QSO formation. As a result of the peculiar steepness of their intrinsic number counts, we find that the lensed source counts at a fiducial wave length of $850\,\mu$m can exceed the unlensed counts by several orders of magnitude at flux densities $\gtrsim100\,$mJy, even with a conservative choice of the maximum magnification.

Key words: gravitational lensing – galaxies: haloes.

1 INTRODUCTION

Gravitational lensing is well known as a powerful tool to probe the overall geometry of the Universe at $z \lesssim 6$; cosmological parameters such as the spatial curvature, the vacuum energy density (described either by a cosmological constant or by a dynamical quantity such as quintessence), and the Hubble constant (Bartelmann et al. 1997; Falco et al. 1998; Cooray 1999; Huterer & Cooray 1999; Macias-Perez et al. 2000; Bhatia 2000; Helbig et al. 2000); the evolution of large scale structure (Rix et al. 1994; Mao & Kochanek 1994; Bacon, Refregier & Ellis 2000); and the masses and the density profiles of dark haloes of galaxies and galaxy clusters (Narayan 1998 and references therein; Mellier 1999; Clowe et al. 2000).

An important effect of gravitational lensing is the possible modification of the observed luminosity functions of distant sources and of their number counts due to the redshift dependent magnification bias (Peacock 1982; Narayan 1989; Schneider 1992).

In this paper we calculate and study the magnification distribution generated by different classes of dark matter haloes (DMH), including both weak and strong lensing. Lenses are distributed following the evolving cosmological DMH distribution (Sheth & Tormen 1999; Sheth, Mo & Tormen 2001). We address the effect of different density profiles of lenses on the resulting magnification: we compare the magnification distribution generated by a population of Navarro, Frenk & White (1997); haloes

★E-mail: perrotta@sissa.it (FP); bacci@sissa.it (CB); msb@mpa-garching.mpg.de (MB); dezotti@pd.astro.it (GDZ); granato@pd.astro.it (GLG)

(NFW haloes) with that generated by singular isothermal spheres (SIS), showing how the different features in the corresponding caustics are reflected in the probability for a given magnification. In both cases, the mass range of the lenses which, as it turns out, contributes most to the magnification bias is that of galaxies.

A similar comparison, but focusing on the angular separation statistics by strong lensing, has recently been performed by Li & Ostriker (2000) and, for generalized NFW profiles, by Wyithe, Turner & Spergel (2001). Whereas the probability distribution of angular separations generated by a population of SIS lenses turns out to be different by orders of magnitude with respect to a corresponding NFW distribution, we find that the magnification distributions instead have very similar amplitudes for a fixed cosmological model. The magnification probabilities differ at most by a factor of ~2 at high magnifications. Indeed, the angular splitting between the brightest images is generally twice the Einstein angle, which can be much larger for galaxy-mass SIS than for NFW lenses of the same mass. Magnification cross-sections behave quite differently, because the lower concentration of NFW haloes is counteracted by a larger area near caustic curves where sources are highly magnified.

On the other hand, it is now well known that neither the simple SIS model nor the NFW are able to reproduce the observed angular-separation statistics of multiply imaged quasars, the former overestimating the occurrence of large angular separations, the latter underestimating the occurrence of small angular separations (Narayan & White 1988; Keeton 1998; Porciani & Madau 2000; Kochanek & White 2001). This confirms the observational evidence that the feedback of baryonic physics is important for the mass distribution in the cores of galaxy-mass lenses.

In order to allow quantitative predictions, we therefore adopt the 'mixed' model by Porciani & Madau (2000), who determined a transition mass separation between the two profiles empirically, taking into account the mass redistribution of galactic DMH due to baryonic infall (Blumenthal & Faber 1986).

We finally apply the magnification probability distribution to the galaxy counts at 850 μm as modelled by Granato et al. (2001). The luminosity function of the source population used here was inferred combining the evolution of the quasi-stellar object (QSO) luminosity function with the relation between the QSOs and the host spheroids, and turns out to fit the SCUBA data. Compared with earlier work by Blain (1996), these source counts are quite a lot steeper than those constructed from models of pure luminosity evolution of the *IRAS* galaxy luminosity function at 60 μm, rescaled to 850 μm, so the effect of lensing turns out to be increased.

Another important quantity entering into the current discussion is the maximum magnification that can be achieved for extended sources. These spheroidal sources do not appear to be point-like, hence the maximum possible magnification is finite. We compute it by means of the ray-shooting method, using a brightness profile appropriate for spheroidal galaxies. Remarkably, this maximum magnification turns out to be quite a lot lower than that used by Blain (1996). However, we show that, because of the peculiar steepness of the intrinsic source counts, even a conservative choice of the maximum possible magnification would give rise to a very high fraction of lensed sources, potentially detectable at fluxes ≳100 mJy.

The plan of this paper is as follows. In Section 2, we introduce the probability for a source at given redshift to be magnified by a certain amount, and quantify the magnification bias on source counts, for which a model is described in Section 4. In Section 3, we briefly describe the mass function adopted for lenses and the density profiles of the lenses. In Section 5, we determine the maximum possible magnification for extended sources. We discuss our results in Section 6, and summarize them in Section 7.

Throughout this paper, Ω_{0m} and $\Omega_{0\Lambda}$ denote the present-day density parameters for the non-relativistic matter and for the cosmological components, respectively, neglecting the radiation energy density. The Hubble constant is $H_0 = 100\,h\,\mathrm{km\,s^{-1}\,Mpc^{-1}}$. Our fiducial model has $h = 0.65$, $\Omega_{0m} = 0.3$, $\Omega_{0\Lambda} = 0.7$ and $\Omega_{0b} h^2 = 0.03$. *COBE* normalization gives $\sigma_8 = \sigma$ ($R = 8\,h^{-1}$ Mpc) $= 0.925$ (Bunn & White 1997). We will concentrate on spatially flat models, and on the filled-beam description of cosmological light propagation.

2   THE MAGNIFICATION DISTRIBUTION

In order to evaluate the effect of magnification by lensing on the counts of a source population, we need to compute the total magnification cross-section of an ensemble of lenses drawn from a given mass function. For a fixed geometry of the lens system, in which the lens and source redshifts are z_s and z_d respectively, the area of the region in the source plane for which the resulting image magnification is larger than μ, is $\sigma(\mu, z_d, z_s, \chi)$, where χ characterizes the lens model (for SIS and NFW lenses, χ could be the virial mass).

The probability of a source at redshift z_s to be lensed with magnification $> \mu$ is obtained by dividing σ_{tot} by the area of the source sphere (e.g. Schneider, Ehlers & Falco 1992),

$$P(\mu, z_s) = \frac{(1 + z_s)^2}{4\pi r^2(z_s)} \int_0^{z_s} dz \frac{dV}{dz} (1 + z)^3$$

$$\times \int dM \sigma(\mu, z, z_s, M) n_c(z, M). \tag{1}$$

In equation 1, $r(z)$ is the comoving radial distance to redshift z, dV/dz is the proper volume element per unit redshift, and $n_c(z,M)$ is the comoving number density of the lenses.

The requirement of non-overlapping cross-sections underlying equation (1) limits its validity to $P \ll 1$, i.e. the total cross-section must be much smaller than the area of the source sphere. The net effect of gravitational lensing on the distribution of flux densities expected from a population of distant sources can be described by the probability distribution of magnifications, $p(\mu, z)$. If $P \ll 1$, the differential probability is $p(\mu, z) = - dP(\mu, z)/d\mu$. The normalization and flux conservation conditions are

$$\int_{\mu_{min}}^{\infty} d\mu\, p(\mu, z) = 1, \qquad \int_{\mu_{min}}^{\infty} d\mu\, p(\mu, z)\mu = 1. \tag{2}$$

Quite independently of the lens model, the differential probability decreases as μ^{-3} for $\mu \gg 1$, hence the high-magnification tail can be written as $p(\mu, z) \propto a(z)\mu^{-3}$. On the other hand, equation (1) breaks down for small magnifications, where multiple lensing events become important and cross-sections begin to overlap (in fact, the probability for many low-magnification lensing events along the line of sight to a source is rather large, while a single interaction producing high magnifications is a relatively rare event). In particular, this implies that there is a critical magnification μ_{cut} below which multiple lensing becomes important, resulting in low-magnification events (weak lensing regime).

Based on general considerations (see Bartelmann & Schneider 2001 for a review), one expects from weak lensing a narrow, slightly skewed magnification distribution with a peak near $\mu = 1$, turning into the high-magnification tail $\propto \mu^{-3}$ at $\mu = \mu_{cut}$.

For a Gaussian density fluctuation field, weak lensing by large-scale structures (e.g. Bartelmann & Schneider 2001; Blandford et al. 1991; Miralda-Escudé 1991; Jain & Seljak 1992; Kaiser 1992) produces a Gaussian magnification distribution. In fact, as long as $\delta\mu \equiv \mu - 1 \ll 1$, the magnification of a source at redshift z can be approximated as

$$\mu(z) = 1 + \delta\mu(z) \approx 1 + 2\kappa(z), \tag{3}$$

i.e. to the first order, the magnification fluctuation is just twice the convergence κ, which itself is a line-of-sight projection of the density contrast δ. The distribution of the magnification fluctuations $\delta\mu$ will then be Gaussian, with mean zero and a dispersion $\sigma_\mu(z)$ which depends on the source redshift and, albeit weakly, on cosmology. Typical values for σ_μ run from $\sim 2 \times 10^{-3}$ for $z = 0.05$ to ~ 0.44 at $z = 7.5$ (cf. Bartelmann & Schneider 2001).

A convenient choice for μ_{cut} is $\mu_{cut} = 1 + 1.5\sigma_\mu(z)$, yielding $\mu_{cut} \approx 1.5$–2 for the redshift range of interest in this paper. We model the probability distribution for $\mu < \mu_{cut}$ as

$$p(\mu, z) = H(z) \exp[-(\mu - \bar{\mu})^2 / 2\sigma_\mu^2(z)], \tag{4}$$

where the precise location of the peak, $\bar{\mu}$, and the amplitude, $H(z)$, are determined by the normalization and flux conservation conditions (equation 2) on the *combined* (weak plus strong lensing) probability distribution.

The magnification probability for isothermal galaxy models has been derived by Peacock (1982) and Vietri & Ostriker (1983) and, for more complicated galaxy models, by Blandford & Kochanek (1987) and Wallington & Narayan (1993). In this paper, we integrate equation (1) also for lenses with NFW density profile, and we describe the low-magnification distribution by equation (4).

We now turn to the magnification bias on a flux-limited source sample. The integrated source counts above a flux density threshold S_ν of sources with a comoving luminosity function $\Phi(L, z)$ can be written as (e.g. De Zotti et al. 1996)

$$N(S_\nu) = \int_0^{z_0} dz \int_{L_{min}}^\infty dL \, \Phi(L, z) r^2(z) \frac{dr}{dz} \, sr^{-1}, \tag{5}$$

where r is the comoving radial distance, and

$$L_{min}(\nu) = 4\pi(1 + z) r^2(z) S_\nu \frac{L(\nu)}{L[(1 + z)\nu]}. \tag{6}$$

The luminosity function modified by the magnification bias reads (e.g. Pei 1995):

$$\Phi'(L, z) = \int_{\mu_{min}}^\infty d\mu \, \frac{p(\mu, z)}{\mu} \Phi\left(\frac{L}{\mu}, z\right). \tag{7}$$

Lensing effects on the source counts are taken into account by replacing $\Phi'(L, z)$ with $\Phi(L, z)$ in equation (5).

3 DMH AS GRAVITATIONAL LENSES

Our goal is to quantify the magnification bias due to virialized DMHs. Therefore, we assume that the lens population consists of collapsed DMH with an epoch-dependent mass function as described by Sheth & Tormen (1999), which fairly accurately

reproduces the results of extensive numerical simulations over more than four orders of magnitude in mass, for a wide range of CDM cosmologies (Jenkins et al. 2001). This function considerably improves upon the familiar Press & Schechter (1974) model, which overestimates the abundance of 'typical' (M_*) haloes and underestimates that of massive systems. The comoving number density of haloes with mass M at redshift z is then

$$\frac{dn}{dM} = \sqrt{\frac{2aA^2}{\pi}} \frac{\rho_0}{M^2} \frac{\delta_c(z)}{\sigma(M)} \left\{ 1 + \left[\frac{\sigma(M)}{\sqrt{a}\delta_c(z)} \right]^{2p} \right\}$$

$$\times \left| \frac{d\ln\sigma}{d\ln M} \right| \exp\left[-\frac{a\delta_c^2(z)}{2\sigma(M)^2} \right]; \tag{8}$$

The best-fitting values of the parameters are $a = 0.707$, $p = 0.3$, and $A \simeq 0.3222$ (Sheth & Tormen 1999; Sheth et al. 2001). The Press–Schechter mass function is recovered for $a = 1$, $p = 0$ and $A = 0.5$.

In equation (8), ρ_0 is the mean mass density at a reference epoch t_0, which we assume to be the present time, and σ^2 is the variance of linear density fluctuations at the present epoch, smoothed with a spherical top-hat filter $W_R(k)$ enclosing mass M. In equation (8), $\delta_c^2(z)$ is the linear density contrast of an object virializing at z, linearly evolved to the present epoch. It can be estimated using the spherical collapse model (e.g. Peebles 1980; Lahav et al. 1991; Lacey & Cole 1993; Nakamura 1996; Eke, Cole & Frenk 1996; Łokas & Hoffman 2001).

Having specified the properties of the lens population, we need to describe the effects of individual lenses on the emitting source.

The ray-tracing equation relates the position of a source to the impact parameter in the lens plane of a light ray connecting source and observer. The light ray passing the lens at an impact parameter ζ is bent by an angle $\hat{\alpha}(\zeta)$. The source position η and the impact parameter ζ in the lens plane are related through

$$\eta = \frac{D_s}{D_d} \zeta - D_{ds} \hat{\alpha}(\zeta), \tag{9}$$

where $D_{d,s,ds}$ are the angular-diameter distances between observer and lens, observer and source, and lens and source, respectively. The deflection angle $\hat{\alpha}$ is the sum of the deflections due to all mass elements of the lens projected on the lens pane, therefore it depends strongly on the lens density profile.

A simple model for the mass profile of a lens (cluster or galaxy) is the singular isothermal sphere (SIS; e.g. Binney & Tremaine 1987). In this lens model, the deflection angle is independent of the impact parameter (cf. Schneider et al. 1992; Narayan & Bartelmann 1997). Because one of the two SIS critical curves degenerates to a point, any given source has either one or two images. Two images appear if, and only if, the source lies inside the Einstein ring.

If all haloes virialize to form singular isothermal spheres, mass conservation implies that the velocity dispersion is related to the mass and overdensity defined in the context of the Press–Schechter theory (see e.g. Kaiser 1986).

The SIS model is useful because it allows one to work out analytically the basic lensing properties. On the other hand, high-resolution N-body simulations (Navarro et al. 1997) showed that in hierarchically clustering universes, a better fit to simulations is provided by the 'universal' density profile (the NFW profile), which is shallower than isothermal near the centre and steeper in

the outer regions:

$$\rho(x) = \frac{\rho_{\text{crit}} \delta_{\text{NFW}}}{x(1+x)^2}, \tag{10}$$

where $x = r/r_s$, r_s is a scale radius depending on the halo mass, δ_{NFW} is the characteristic density contrast of the halo, and ρ_{crit} is the critical density at the epoch of halo virialization.

N-body simulations with yet higher resolution indicate a steeper central cusp than that of the NFW profile, $\rho(x) \propto [x^{1.5}(1+x)^{1.5}]^{-1}$ (Moore et al. 1999; Ghigna et al. 2000). Because the slope of the central density profile in this case [$\rho(r) \propto r^{-1.5}$] falls between the NFW [$\rho(r) \propto r^{-1}$] and the SIS [$\rho(r) \propto r^{-2}$] slopes, the two cases considered here (NFW and SIS) will bracket it.

We parametrise haloes by their virial mass M, enclosed in a radius r_Δ (the radius of a sphere with mean interior density $\Delta\rho_{\text{crit}}$; see Eke, Navarro & Steinmetz 2001). The halo concentration is $c = r_\Delta/r_s$, and it increases with decreasing halo mass. It is related to the density parameter δ_{NFW} by

$$\delta_{\text{NFW}} = \frac{\Delta}{3} \frac{c^3}{[\ln(1+c) - c/(1+c)]}. \tag{11}$$

The virial radius of a halo at redshift z depends on the halo mass as

$$r_\Delta = \frac{0.95 \times 10^{-1}}{\Delta^{1/3}(1+z)} \left(\frac{M}{h^{-1}\,\text{M}_\odot}\right)^{1/3} \left[\frac{\Omega_{0m}}{\Omega_m(z)}\right]^{-1/3} h^{-1}\,\text{kpc}. \tag{12}$$

For a given halo mass, equations (12) and (11) completely specify the density profile (equation 10).

The lens equations for the NFW profile are given by Bartelmann (1996), Maoz et al. (1997) and Wright & Brainerd (2000). While the SIS profile has only one critical curve of finite extent, the NFW has two, hence it has either one or three images. We will see in Section 6 how the number and radius of critical curves relates to the total magnification distribution.

4 SOURCE COUNTS IN THE SUBMILLIMETRE WAVEBAND

We compute the lensing effects on 'unlensed' galaxy counts in the submillimetre waveband taken from the model by Granato et al. (2001), which is in good agreement with the available SCUBA data at 850 μm (Blain et al. 1999; Smail et al. 1999).

In this model the rate of formation of spheroids at high redshift is estimated exploiting (i) the QSO luminosity function and (ii) the observational evidence, leading to the conclusion that high redshift QSOs did shine in the core of early-type proto-galaxies during their main epoch of star formation. In this scenario the star formation is more rapid in more massive objects, ranging from ~0.5 to ~2 Gyr when going from more-massive to less-massive objects. This *anti-hierarchical baryonic collapse* is expected to occur in DMH, when the processes of cooling and heating are considered. The larger the dark halo and the enclosed spheroid masses are, the shorter the gas infall and cooling times will be, leading to a faster formation of the stars and of the central black hole. The star formation process and the quasar shining phase proceed until powerful galactic winds are driven by the quasar itself, which occurs at a characteristic time when its luminosity becomes high enough. In order to account for the observed statistics of QSOs and elliptical galaxies in the framework of hierarchical structure formation, Monaco, Salucci & Danese (2000) also introduced a time lag between the beginning of the star formation and the QSO bright phase which decreases with mass.

The spectroscopic evolution of the galaxies adopted here is based on the GRASIL model (Silva et al. 1998). It includes (i) chemical evolution; (ii) dust formation, assumed to follow the chemistry of the gas; (iii) integrated spectra of simple stellar populations (SSP) with the appropriate chemical composition; (iv) a realistic 3-dimensional distribution of stars, molecular clouds (in which stars form and subsequently escape), and diffuse dust; and (v) radiative transfer computation in this clumpy interstellar medium (ISM) and dust temperature distribution determined by the local radiation field.

With these ingredients, the evolving luminosity functions (LF) at various wavelengths in the millimetre and submillimetre wavebands are evaluated numerically, and they turn out to be significantly different from pure luminosity evolution models for the 60 μm LF of *IRAS* galaxies (Saunders et al. 1990), properly rescaled to the wavelengths of interest. The *IRAS* galaxy LF, which is based on an empirical model describing the evolution in a parametric way, was used by Blain (1996) to obtain galaxy counts in the submillimetre wavebands, which were then used for estimating the incidence of gravitational lensing on source counts. However, the model by Granato et al. implies steeper source counts, nearly exponentially decreasing at bright fluxes, so that the effect of gravitational lensing is expected to be more important.

In all source counts obtained in this paper, with and without magnification bias, the spheroids include elliptical galaxies as well as bulges of Sa galaxies, and we followed the formalism of Granato et al. (2000) on the source properties.

5 MAXIMUM MAGNIFICATION FOR EXTENDED SOURCES

As discussed by Peacock (1982), magnification cannot be arbitrarily large for extended sources. Correspondingly the magnification distribution must be cut off at large μ as:

$$p(\mu) \propto \exp\left(-\frac{\mu}{\mu_{\text{max}}}\right), \tag{13}$$

where the cut-off magnification μ_{max} depends on the physical size of the source.

Because in some applications, e.g. for estimating the influence of lensing on counts of submillimetre sources (Blain 1996), the results are sensitive to the adopted value of μ_{max}, the approximated expression derived by Peacock (1982) [$\mu_{\text{max}} = 70(DH_0/c) \times (d/h^{-1}\,\text{kpc})^{-1}$, where d is the physical radius of the source, D is the angular diameter distance of the source and c/H_0 is the Hubble radius] may not be sufficient.

The morphology of strongly lensed sources indicates that most lenses are not circularly symmetric (e.g. Narayan & Bartelmann 1997 and references therein). Therefore, to estimate the maximum possible magnification for a source of physical radius r at redshift z_s, we consider in general an elliptical lensing potential due to a quasi-isothermal sphere (Blandford & Kochanek 1987). Defining polar coordinates r and θ in the image plane, centred on the centre of mass, and measuring θ from the major axis of the ellipse, the deflection potential may be written as

$$\Psi(r, \theta) = \theta_E \sqrt{(s^2 + r^2)}(1 - g\cos 2\theta). \tag{14}$$

Here, g is the ellipticity parameter, s is the core radius, and θ_E is the Einstein angle. The results for an extended source depend only weakly on s, within a relatively broad range; we thus set $s = 0$ for simplicity in the following.

Using this potential, we compute by means of the ray-shooting method (e.g. Schneider et al. 1992, p. 304) the expected magnification $\mu(\mathbf{y})$ of a point-like source as a function of its position $\mathbf{y}$ in the source plane. Then, the magnification of an extended source with brightness profile $I(\mathbf{y})$, as a function of the distance $\mathbf{y}_E$ from its centre, is given by

$$\mu_E(\mathbf{y}_E) = \frac{\int I(\mathbf{y})\mu(\mathbf{y})\,d^2 y}{\int I(\mathbf{y})\,d^2 y}. \tag{15}$$

For the brightness profile, we have use either a De-Vaucouleurs law;

$$\log I(R) = \log I_e - 3.33[(R/R_e)^{1/4} - 1], \tag{16}$$

or a Hubble profile;

$$I(R) = I_0/(1 + R/R_0)^2. \tag{17}$$

Observed profiles of spheroidal galaxies are well reproduced by both functional forms over a wide range of R, provided $R_e \simeq 11 R_0$ (Mihalas & Binney 1981).

Adopting this relation between the scalelengths, we find that the estimated μ_E are very similar for both profiles. Therefore, we present only results for equation (16) in the following. We choose $R_e = 5\,h^{-1}\,\text{kpc}$ as a typical scale radius for a bright elliptical galaxy (e.g. Kent 1985). For a SIS, the maximum possible magnification is achieved when the lens is close to the observer, i.e. when $D_{ds} \approx D_s$. We set $\sigma_v = 300\,\text{km s}^{-1}$, which corresponds to a mass within $25\,h^{-1}\,\text{kpc}$ radius of $10^{12}\,\text{M}_\odot$, following the isothermal relation $M(<R) = 2\sigma_v^2 R/G$. With our choice of the cosmological model, the Einstein angle is $\theta_E = 2.6\,\text{arcsec}$.

Fig. 1 shows the magnification for an extended source, μ_E, as a function of the separation r of its centre from the projection of the lens centre into the source plane. For the figure, we put $g = 0$ in equation (14) i.e. (we adopted a spherical potential) and the source is at $z_s = 3$, but very similar figures are obtained for $1 \le z_s \le 4$. The figure shows that the magnification is maximized when source and lens are aligned, then $\mu_{max} \simeq 26$. If the lens is placed instead at $z_l = 0.5$, then $b = 1.2\,\text{arcsec}$ and $\mu_{max} \simeq 13$.

However, as already remarked, strongly lensed sources are usually interpreted in terms of lensing potentials with non-vanishing ellipticity. A typical value for g could be 0.1. In this case, the symmetry of μ_E around $r = 0$ is broken, the maximum magnification $\mu_{max} \simeq 12$ is significantly lower than in the spherical case, and occurs when the lens and the source are offset by $\sim 0.7\,\text{arcsec}$ along the major axis of the ellipse. The results are detailed in Fig. 2.

We conclude that reasonable values of μ_{max} for extended sources are in the range 10–30 for sources in the redshift range 1–4 with effective radii of $1 \lesssim R_e/(h^{-1}\,\text{kpc}) \lesssim 10$. A value of 10 is a fairly conservative lower limit, easily exceeded for a wide range of the relevant parameters, while a value of 30 is obtained only under favourable conditions.

6 NUMERICAL RESULTS AND DISCUSSION

6.1 Relevant masses

In principle, the individual lenses are represented here by dark matter haloes with masses of 10^9–$10^{15}\,\text{M}_\odot$, including galaxies as well as galaxy clusters. However, there is a narrower mass range relevant for gravitational lensing. The optical depth for a beam of
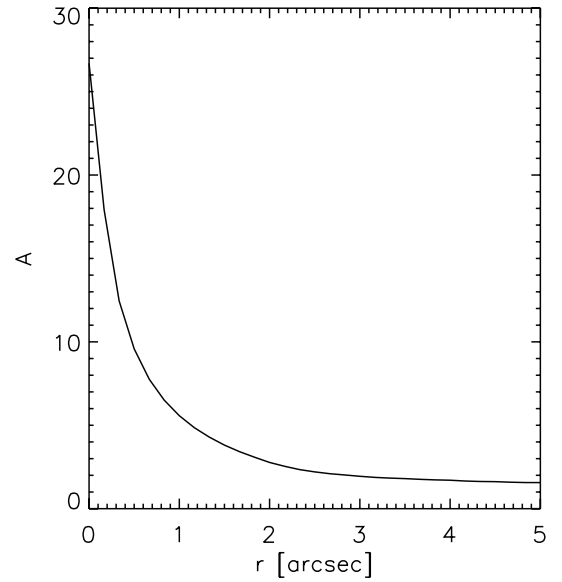
Figure 1. Magnification of an extended source as a function of the offset r between its centre and the projection of the lens centre in the source plane. Here the lens potential is axially symmetric. See text for details.
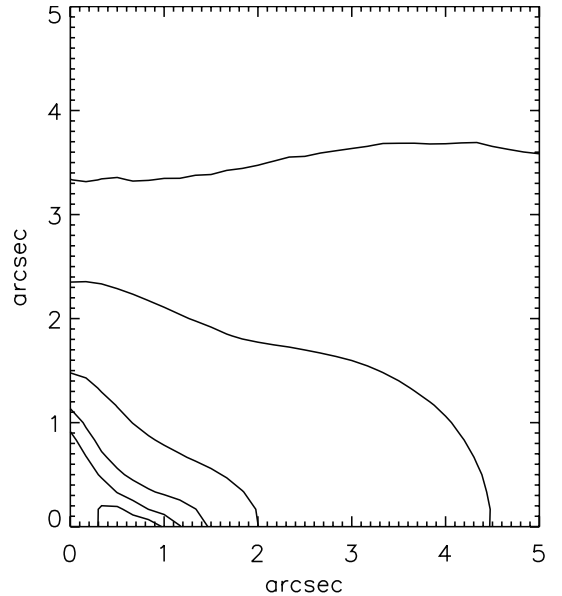

Figure 2. Contour plot of the magnification for an extended source when $g = 0.1$. The projection of the lens centre in the source plane is at the origin of axes. The levels are at $\mu = 1.5, 2, 4, 6, 8$ and 10 from outside in. See text for details.

light from a source due to lensing is proportional to the number density of deflectors multiplied by the cross-section for a given magnification, integrated along the line of sight. Two competing effects are thus important. First, the path length to a source is larger for a Λ cold dark matter (ΛCDM) model. Secondly, the structure formation histories within the standard hierarchical clustering scenario are also different for the different cosmologies. If we normalize the models to reproduce the local cluster abundance, the density of objects less massive than clusters is lower in the ΛCDM model, because the mass function is flatter (e.g. Eke et al. 1996). This is shown in the upper panel of Fig. 3, where the mass function (8) is plotted as a function of the halo mass at $z = 0$. The
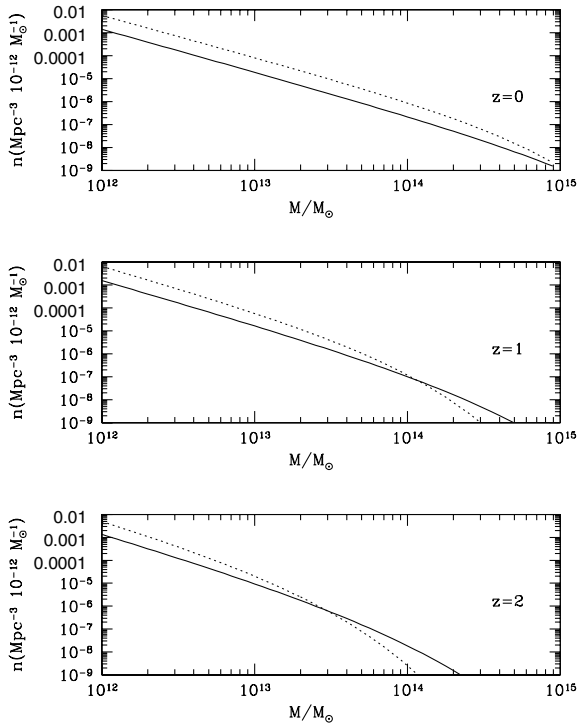
Figure 3. The Sheth & Tormen (1999) mass function for a flat CDM model (dotted line) and for a ΛCDM model (solid line), at redshifts $z = 0, 1, 2$, respectively, from top to bottom.
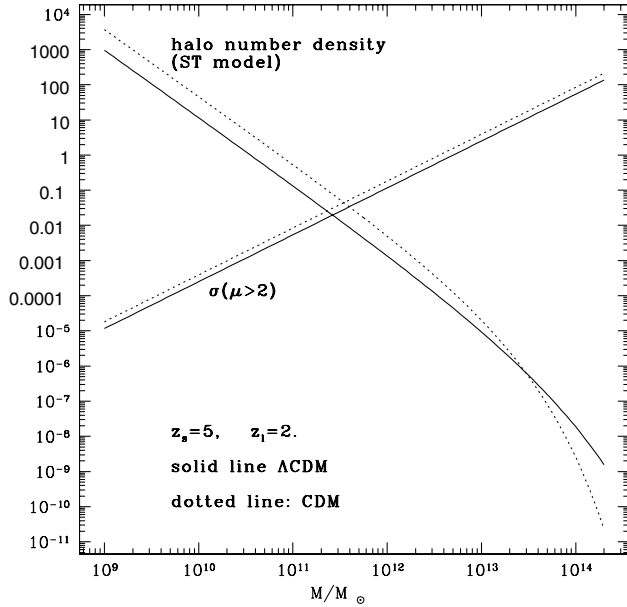

Figure 4. Number density of dark-matter haloes [from the Sheth & Tormen (1999) mass function], and cross-section for magnification $\mu > 2$ by an SIS lens, in arbitrary units, as a function of the lens mass in $M_\odot$. Dotted lines correspond to flat CDM, solid lines to ΛCDM, both normalized to the local cluster abundance.

number of low-mass objects keeps increasing with redshift above the ΛCDM model, whereas the opposite is true for high masses. The next question is then: which is the mass range contributing most to the optical depth? In Fig. 4, we show, as a function of the lens mass, both the cross-section for magnifications $\mu > 2$ and the lens mass function for fixed values of the source and lens redshifts.
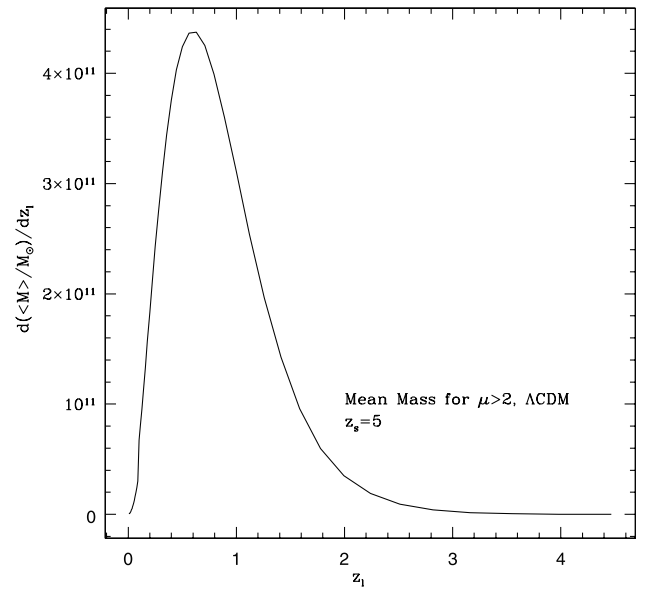

Figure 5. Contributions from different redshifts to the effective lens mass (see text) for a fixed configuration of the lens system, SIS lenses, and a ΛCDM model.
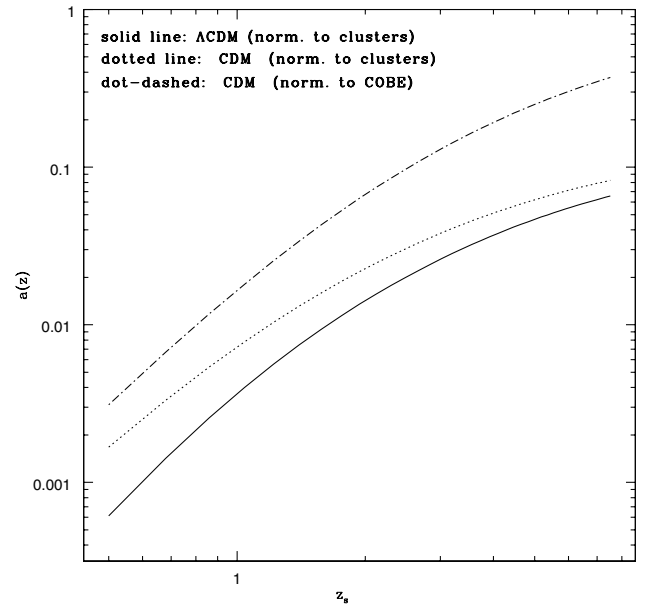

Figure 6. SIS model: comparison of the high-magnification tail amplitudes $a(z)$ for a flat ΛCDM model with $\Omega_{0\Lambda} = 0.7$ (solid line), and a flat CDM model (dotted line), both normalized to the local cluster abundance. The amplitude is plotted vs. source redshift. The dot-dashed line refers to a *COBE*-normalized flat CDM universe.

An SIS lens profile is adopted. It may be noted that the magnification cross-section is similar for the two models (although slightly higher for the flat CDM model). The product of the two functions peaks at masses between 10^{11} and $10^{12}\,M_\odot$ for both a flat CDM and a ΛCDM model.

The effective mass of dark matter haloes contributing most to strong lensing of a source located at z_s can be estimated as:

$$\langle M \rangle = \int \mathrm{d}z_l \int \mathrm{d}M M \frac{\mathrm{d}P(\mu, z_s)}{\mathrm{d}z_l \mathrm{d}M}, \tag{18}$$

where $P(\mu, z_s)$ is the cumulative probability of magnification $> \mu$. The inner integral, $d\langle M \rangle / dz_l$, is plotted in Fig. 5 as a function of z_l, for $z_s = 5$, a SIS lens profile and a ΛCDM model. As illustrated there, the maximum contribution to the magnification probability comes from the mass range $(10^{11} - 10^{12} \, M_\odot)$, for which space densities implied by a CDM model are appreciably higher than in the case of a ΛCDM model (in the relevant redshift interval) if the models have to be consistent with the observed cluster abundance. This more than compensates for the larger path length to a source in a ΛCDM model and explains why the probability distribution of strong magnifications has a *lower* amplitude in this model. To illustrate the effect of the normalization of the primordial fluctuations on the resulting magnification probability distribution $p(\mu, z)$, we plot in Fig. 6 the amplitude $a(z)$ of the high-magnification tail for two different cosmologies, viz. a flat CDM and a ΛCDM model with $\Omega_{0\Lambda} = 0.7$ and $\Omega_{0m} = 0.3$. We have adopted SIS profiles for the lenses. The two models are normalized to reproduce the local abundance of rich clusters, $\sigma_8 = 0.56\Omega_{0m}^{-0.47}$ (e.g. Viana & Liddle 1999).

Also shown in Fig. 6 is the amplitude $a(z)$ for a *COBE*-normalized standard CDM model. The relatively large values for this quantity for any source redshift are unrealistic, as they are a result of a mass function of dark haloes inconsistent with the cluster abundance. This figure is consistent with the recent analysis by Li & Ostriker (2000).

6.2 SIS versus NFW profiles

Fig. 7 compares the effect of SIS and NFW lens profiles on the magnification distributions for sources at $z_s = 4$ and $z_s = 7$, including the weak lensing effect for $\mu < \mu_{cut}$. The magnification distributions are obtained by integrating the cross-sections in the source plane over lens masses, weighted by the mass distribution (8). The weak-lensing regime, responsible for magnifications below μ_{cut}, gives rise to a Gaussian peak near $\mu = 1$ the dispersion of which increases with increasing source redshift. The high-magnification tail of Fig. 7 is shown in closer detail in Fig. 8. Note
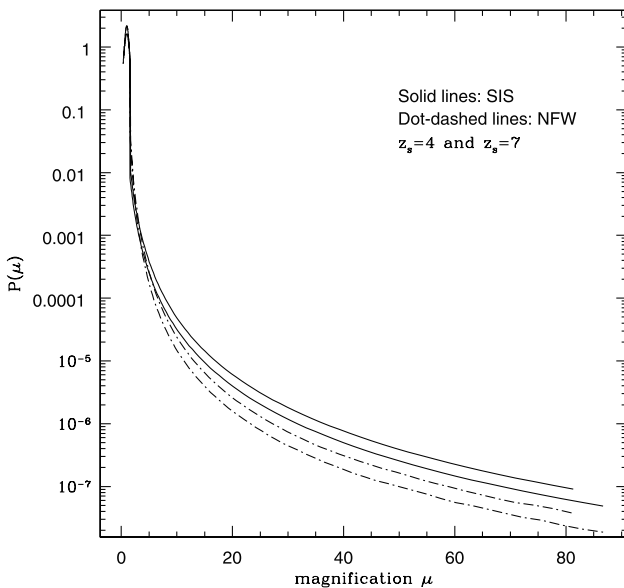
that the plotted distribution of magnifications has a discontinuity in μ_{cut}, i.e. at the transition between the weak and strong lensing regimes.

The two density profiles lead to slightly different magnification distributions. In particular, the NFW lens is more efficient than the SIS for moderate magnifications $(2 \lesssim \mu \lesssim 4)$, and less efficient for high magnifications. In fact, NFW lenses have smaller high-magnification cross-sections than SIS lenses of equal mass, even if the average magnification is higher. This can be seen in Fig. 9, where we plot the cross-section for magnifications $\mu > 2$ and
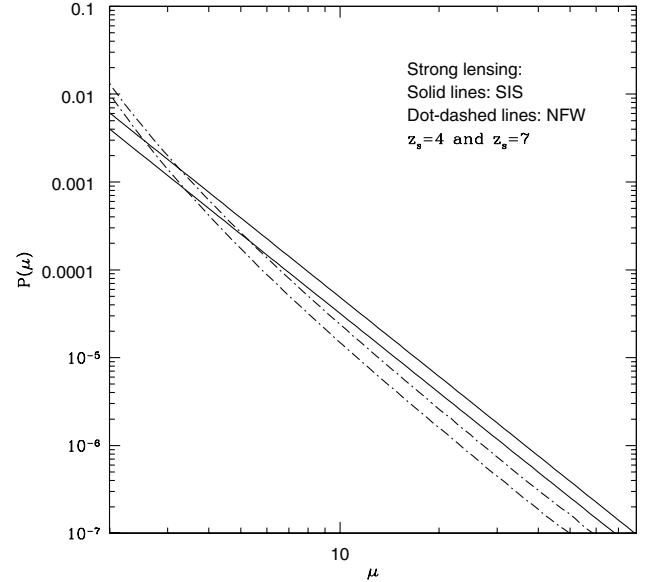

Figure 8. High-magnification tail of $P(\mu)$. Magnifications are plotted on a logarithmic scale. The plots refer to populations of SIS (solid lines) and NFW lenses (dot-dashed lines) for sources at redshifts $z_s = 4$ (lower curves) or at $z_s = 7$ (upper curves).
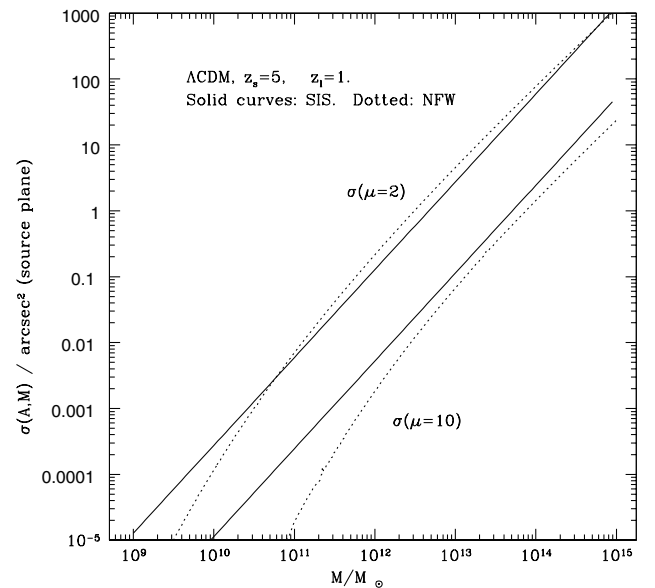

Figure 7. Magnification distribution from a population of SIS (solid lines) and NFW lenses (dot-dashed lines) for sources at redshifts $z_s = 4$ (lower curves) and $z_s = 7$ (upper curves).

Figure 9. Magnification cross-sections $\sigma(\mu)$ (in square arcsec) for $\mu > 2$ (upper curves) and $\mu > 10$, as a function of the halo mass. The sources are at $z_s = 5$ and the lenses at $z = 1$. The cross-sections are plotted for SIS (solid lines) and NFW haloes (dotted lines).

$\mu > 10$ as a function of the halo mass for the two models, keeping the configuration of the system fixed. For virtually all halo masses, $\sigma(10)_{\mathrm{NFW}} < \sigma(10)_{\mathrm{SIS}}$, while $\sigma(2)_{\mathrm{NFW}} > \sigma(2)_{\mathrm{SIS}}$. Even though the latter relation fails for very small lens masses, it still holds when the cross-sections are weighted with the appropriate mass function. As mentioned above, the bulk of the contribution to the magnification distribution comes from a limited mass range. The effective mass defined in Section 6.1 is nearly equal for SIS and NFW profiles, namely $\sim 10^{11}$–$10^{12}\,\mathrm{M}_\odot$. Although $\langle M \rangle$ depends (albeit weakly) on the lens redshift, massive clusters never contribute substantially to the integrand in equation (1) because they are extremely rare.

As a useful example, let us consider a $10^{12}\,\mathrm{M}_\odot$ object, described as an SIS or as an NFW lens. The convergence κ for the two profiles is shown in the upper panel of Fig. 10 as a function of halo-centric distance (the virial radius is approximately $r_\Delta \simeq 140\,h^{-1}$ kpc). Here, the lens is at $z_l = 1$ and the source is at $z_s = 5$. The two convergence profiles are quite similar, but the shear is also playing a fundamental role to determine the magnification distribution. In the lower panel of Fig. 10, we plot, for the two profiles, $\det^{-1}\mathcal{A}$, i.e. the image magnification μ of an image with impact parameter r in the lens plane. The critical curves behave differently: even though the NFW profile has a singular core, it has tangential and radial critical curves (Bartelmann 1996), while the SIS has only a tangential critical curve (whose caustic degenerates to a point for all axially symmetric lenses). Consequently, the maximum image number is two for SIS and three for NFW lenses.

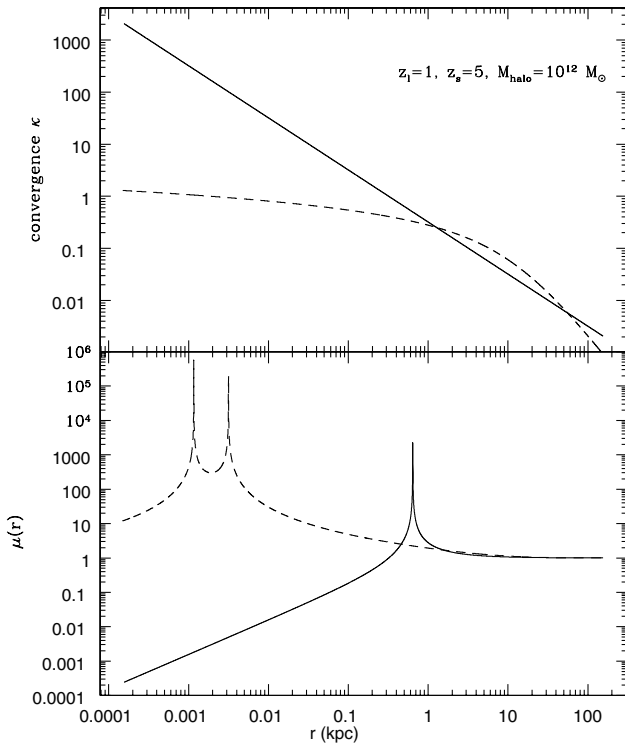Fig. 10 shows that the tangential critical curve of a SIS is located at a larger radius than both critical curves of an NFW halo with equal mass. This means that high magnifications are favoured in the SIS model, because the corresponding cross-sections in the source plane is larger. On the other hand, the SIS profile yields lower total magnifications when the source lies well outside the outer caustic in the source plane. The NFW cross-sections for $\mu_{\mathrm{tot}} \sim 2$ generally exceed those of the SIS, because of the fact that the lensing potential is flatter for the NFW than for the SIS profile. Hence this also holds for more massive haloes.

For comparison, let us now consider the equilibrium configurations for a $10^{14}\,\mathrm{M}_\odot$ halo, whose virial radius is approximatively $r_\Delta \simeq 690\,h^{-1}$ kpc.

In Fig. 11, we plot the convergence and the magnification for a single image as a function of its distance from the optical axis. After adding the absolute magnifications of all images, inverting to find the cross-section $\sigma(\mu)$ as a function of source position, and integrating over all lenses up to the source redshift, this explains the enhancement of the NFW probability for low magnifications with respect to the SIS model, shown in Fig. 7, and the opposite effect for large magnifications. However, we see that the probability distributions are quite similar and the effects of lensing on a source population turn out to be nearly insensitive to the specific density profile adopted (at least in the two cases we studied). A completely different result would be obtained when dealing with lensing probabilities of splitting angles in multiple imaging produced by the same lens models. As discussed in detail by Li & Ostriker (2000), the latter distribution can differ by orders of magnitude, depending on the separation angle. Angular splitting is generally of the order of twice the Einstein angle, which for a

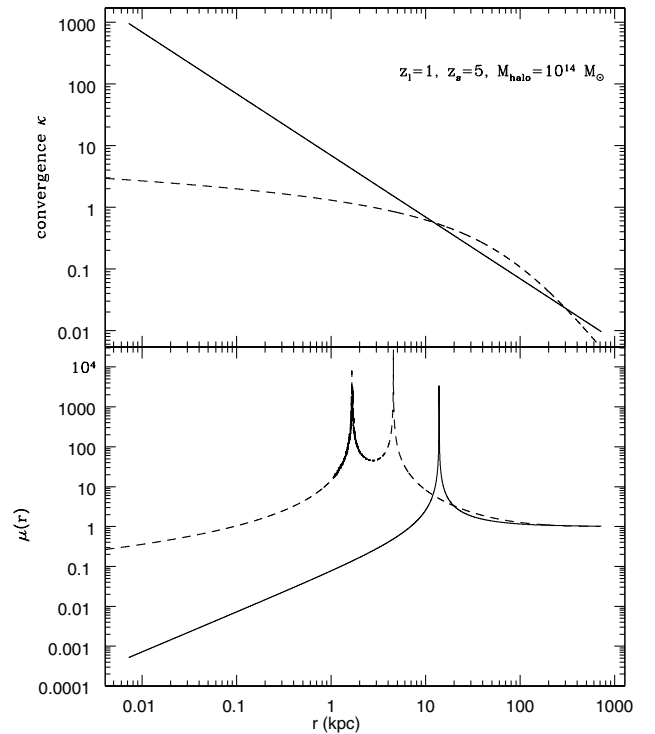**Figure 10.** Upper panel: convergence κ as a function of halo-centric distance for a halo with $M_{\mathrm{halo}} = 10^{12}\,h^{-1}\,\mathrm{M}_\odot$ at $z_l = 1$. The sources are at $z_s = 5$. The plot refers to an SIS (solid line) or an NFW halo (dashed line). Lower panel: magnification of the single image as a function of impact parameter, involving convergence and shear of the gravitational field (see text).

Figure 11. Upper panel: convergence κ as a function of halo-centric distance for a halo with $M_{\mathrm{halo}} = 10^{14}\,h^{-1}\,\mathrm{M}_\odot$ at $z_l = 1$. The sources are located at $z_s = 5$. The plot refers to an SIS (solid line) or an NFW halo (dashed line). Lower panel: magnification of the single image as a function of impact parameter, involving convergence and shear of the gravitational field.

galaxy modelled as a SIS is much larger than for an NFW galaxy with the same mass. Conversely, magnification cross-sections turn out to be more sensitive to the number and extent of finite critical curves, so that the lower central concentration of an NFW profile is counterbalanced by the additional critical curve.

We finish with a cautionary note. The simulations resulting in the density profile of equation (10) did not have sufficient resolution for halo masses $\lesssim 10^{10} h^{-1} \, M_\odot$. Thus, when calculating $p(\mu,z)$ from a NFW lens population with masses $\gtrsim 10^9 \, M_\odot$, we are arbitrarily extrapolating the validity of this density profile, as well as the relation between halo concentration and mass, to a mass range where higher-resolution N-body simulations would be required. Furthermore, as pointed out in Porciani & Madau (2000) and Kochanek & White (2001), a SIS population would overestimate the number of large angle image splitting of QSOs, while a NFW model is unable to explain the observed small-angle separation tail of the probability distribution of image splitting.

In order to obtain agreement with the data on image separations of QSOs, baryonic cooling in dark matter haloes, which is able to transform NFW haloes into isothermal distributions for masses smaller than some threshold must be taken into account. In such a picture, DM haloes are modelled as NFW haloes only above a threshold that is certainly well above the smallest mass that we are considering here. Therefore, the purely SIS or purely NFW probability distributions derived here are not good for many practical purposes. Rather, our analysis showed that, in contrast to angular separation distributions, the magnification distribution is not as nearly as strongly affected by the difference in the two density profiles, yielding only differences by a factor of ~ 2 at high magnifications (as Fig. 8 shows). However, in order to draw observational constraints, we will follow Porciani & Madau (2000) and adopt their 'mixed' model. The lenses will be modelled as SIS below $\sim 10^{13} \, M_\odot$, and as NFW haloes otherwise (the value of this transition mass was found empirically, and it gives the best fit to the angular separation observed in the CASTLE survey (http://cfa-www.harvard.edu/castles/). As obvious, the magnification distribution for such a mixed model will average between the SIS and NFW distributions plotted in Fig. 8, while the respective angular separations will substantially differ. An application of this 'mixed' model will be the subject of next section.

6.3 An application: effects on the source counts

As an example of magnification bias from strong lensing on high-redshift sources, we apply our predictions of the magnification distribution to the sources modelled by Granato et al. (2000) and described in Section 4. Using the 'corrected' magnification distribution $p(\mu)$ for extended sources, equation (13), we compute lensed counts at $850 \, \mu m$ using the 'mixed' model described in the previous section and compare them with the 'unlensed' and weakly lensed counts. In Fig. 12, the solid line shows the integral source counts that we expect at $850 \, \mu m$ from the source distribution described in Section 4, ignoring lensing. The dot-dashed line includes only weak lensing, using the low-magnification tail of the magnification distribution $p(\mu,z)$. Because the latter is modelled as a Gaussian with small dispersion around the mean, we can see from Fig. 12 that weak lensing by large-scale structures has very little effect on the integral source counts, even though the variance of the distribution increases with source redshift. The weakly lensed counts are therefore quite similar to the unlensed ones given by Granato et al. (2000). Even the weakly lensed counts, however, fall
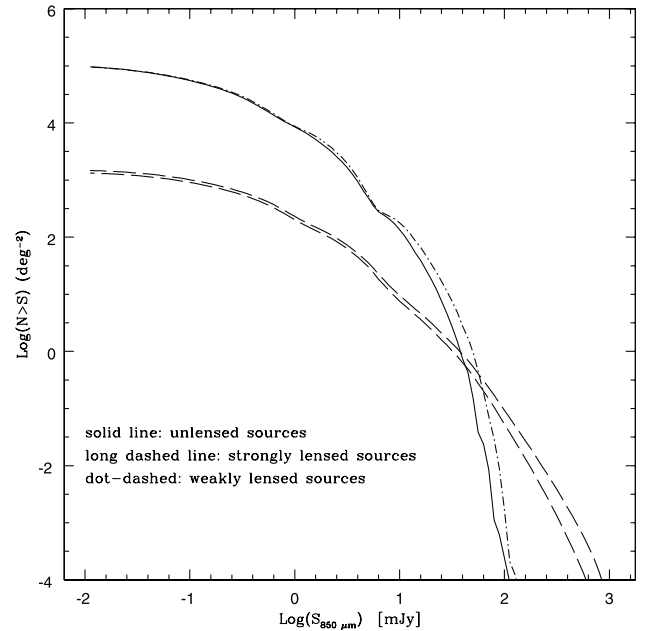

Figure 12. Integral source counts at $850 \, \mu m$ per square degree. Unlensed counts are given by the solid line, and counts including weak lensing by the dot-dashed line. Short-dashed lines show, for the SIS model, strongly lensed source counts with $\mu_{E,max} = 10$ (lower short-dashed lines) or $\mu_{E,max} = 30$ (upper short-dashed lines), as described in the text. Long-dashed lines are the same for the NFW lens model.

above the unlensed counts where the number-count function falls most steeply.

The effects of strong lensing by a Sheth & Tormen (1999) mass distribution of haloes are plotted in Fig. 12 as long-dashed lines, for $\mu_{E,max} = 10$ (lower line) and $\mu_{E,max} = 30$ (upper line). We can see that the relative contribution of strong lensing is of the order of 10^{-2} in the flat part of the counts, while it dramatically increases in the steepest region, overcoming the weakly lensed counts. This is due to the very strong magnification bias for these sources. First, the typical source redshift ($3 \leq z \leq 5$) is quite high in this source model (increasing the probability for a source to undergo a strong lensing event). Secondly, and importantly, the steep source counts, as discussed by Blain (1996), provide a huge reservoir of sources to be magnified above the flux limit of the observation. Note the remarkable steepness of the counts at $850 \, \mu m$, due to the peculiar properties of this model (i.e., spheroid formation rate and spectroscopic evolution of galaxies).

At flux densities around $100 \, mJy$, the counts are dominated by sources magnified by a factor $\mu \sim 10$–20. At higher flux densities, lensed sources are reduced by the effect of the magnification cut-off at $\mu_{E,max} = 30$. Remarkably we find that, even with a conservative assumption about the maximum magnification allowed (i.e., $\mu_{max} = 10$), there is a large ratio of lensed/unlensed sources at fluxes $\gtrsim 100 \, mJy$, due to the peculiar steepness of the counts predicted by Granato et al. (2000). The substantial magnification bias at flux densities around $100 \, mJy$ not only allows the detection of sources otherwise too faint for detection, but may also allow the discrimination between different models of galaxy formation, depending on the ratio of lensed/unlensed sources detected. Furthermore, this result may have very interesting consequences on the expected number of SCUBA sources to be found in the whole sky maps to produced by the upcoming Planck Surveyor Satellite, operating at nine frequency

channels between 0.3 and 10 mm (Mandolesi et al. 1998). This issue will be studied in detail in a forthcoming paper (Perrotta et al., in preparation).

7   SUMMARY AND DISCUSSION

Gravitational lensing effects, mainly arising from high-redshift emitting sources such as QSOs, have been proved to contain a great deal of information, both cosmological and astrophysical. In particular, as outlined by Blain (1996), the magnification bias exerted by intervening dark-matter haloes can very efficiently increase the number counts of observable submillimetre sources, due to their particularly steep slopes. In this paper, we extend earlier studies of the magnification bias on high-redshift sources (Blain 1996) in three different directions:

(i) We model in detail the magnification distribution expected from a cosmological distribution of dark matter haloes which have either a singular isothermal profile or an NFW profile, which is flatter than isothermal near the core and steeper outside. For the mass function of the haloes, we use the Press−Schechter function, modified for elliptical collapse by Sheth & Tormen (1999).

Whereas the magnification cross-section of the singular isothermal sphere are straightforward and well known, we compute for the first time the magnification distribution for NFW lenses. We find that the integrated magnification distribution of a cosmological ensemble of lenses depends only very weakly on the dark-matter profile, which is in pronounced contrast to the integrated angular-separation distribution, which is substantially lower for a population of NFW haloes than for a population of singular isothermal spheres (e.g. Li & Ostriker 2000).Therefore, how the lenses are modelled in detail is quite irrelevant for the magnification bias on source counts which removes substantial uncertainty from earlier estimates. We emphasize that we are not concerned with the image splitting statistics caused by galaxies, in the cores of which baryonic processes can alter the density profile considerably. Our findings show that, for our purposes, it is unimportant whether the lens population consists of galaxies with singular isothermal profiles or dark-matter haloes with comparatively flatter cores, or a mixture thereof.

(ii) We also model in detail the impact on the magnification bias of the finite extent of the sources, which imposes an upper limit on the magnification because the magnification distribution of the lenses then has to be convolved with the brightness profile of the sources. We show that the maximum magnifications for sources with de Vaucouleurs and Hubble profiles are very similar, provided the profile parameters are suitably chosen to reproduce the brightness profiles of spheroidal galaxies. We find that maximum magnifications between 10 and 30 can be achieved assuming sources with effective radii R_e between 1 and $10\,h^{-1}$ kpc, where 10 is conservative and 30 is achieved only under favourable conditions.

(iii) As an important application of this study, we analyse the effects of magnification bias on submillimetre source counts. Instead of the empirical submillimetre source-count model based on the *IRAS* galaxy luminosity function used in the earlier study by Blain (1996), we use the model by Granato et al. (2001) based on the QSO population at high redshift. This model is augmented by a model for the spectroscopic evolution of galaxies (GRASIL; Silva et al. 1998) and reproduces the SCUBA data at 850 μm well.

This model results in a steeper source-count function than that used by Blain, and therefore leads to an increased magnification bias. This is important for upcoming full-sky surveys in the submillimetre regime, such as the *Planck* mission which is expected to observe a large number of such sources.

In summary, we find that the magnification bias by dark matter haloes on high-redshift sources is quite independent of whether the haloes are modelled as singular isothermal spheres or NFW lenses, and that lensed sources can dominate the submillimetre source counts at fluxes above ∼100 mJy. The influence of the exact value of the maximum magnification is relatively minor and gives rise to an uncertainty of about a factor of two.

REFERENCES

Bacon D. J., Refregier A. R., Ellis R. S., 2000, MNRAS, 318, 625
Bartelmann M., 1996, A&A, 313, 697
Bartelmann M., Schneider P., 2001, Phys. Rep. 340, 291
Bartelmann M., Huss A., Colberg J. M., Jenkins A., Pearce F. R., 1997, A&A, 330, 1
Bhatia V. B., 2000, Proc. IAU Symp. 201, New Cosmological Data and the Values of the Fundamental Parameters. Astron. Soc. Pac., San Francisco
Binney J., Tremaine S., 1987, Galactic Dynamics. Princeton Univ. Press, Princeton
Blain A. W., 1996, MNRAS, 283, 1340
Blain A. W., Ivison R., Kneib J. P., Smail I., 2000, in Bunker A. J., van Breugel W. J. M., eds, ASP Conf. Ser. Vol. 193, The High-Redshift universe: galaxy formation and evolution at high redshift. Astron. Soc. Pac., San Francisco
Blandford R. D., Kochanek C. S., 1987, ApJ, 321, 658
Blandford R. D., Saust A. B., Brainerd T. G., Villumsen J. V., 1991, MNRAS, 251, 600
Blumenthal G. R., Faber S. M., 1986, ApJ, 301, 27
Bunn E. F., White M., 1997, ApJ, 480, 6
Clowe D., Luppino G. A., Kaiser N., Gioia I. M., 2000, ApJ, 539, 540
Cooray A., 1999, ApJ, 512, 83
De Zotti G., Franceschini A., Toffolatti L., Mazzei P., 1996, Astron. Lett. Commun., 35, 289
Eke V. R., Cole S., Frenk C. S., 1996, MNRAS, 282, 263
Eke V. R., Navarro J. F., Steinmetz M., 2001, ApJ, 554, 114
Falco E. E., Kochanek C. S., Muñoz J. A., 1998, ApJ, 494, 47
Ghigna S., Moore B., Governato F., Lake G., Quinn T., Stadel J., 2000, ApJ, 544, 616
Granato G. L., Silva L., Monaco P., Panuzzo P., Salucci P., De Zotti G., Danese L., 2001, MNRAS, 324, 757
Helbig P. et al., (the Jvas/Class team), 2000, Proc. IAU Symp. 201, New Cosmological Data and the Values of the Fundamental Parameters. Astron. Soc. Pac., San Francisco, in press
Huterer D., Cooray A. R., 1999, A&AS, 194, 9003
Jain B., Seljak U., 1997, ApJ, 484, 560
Jenkins A., Frenk C. S., White S. D. M., Colberg J. M., Cole S., Evrard A. E., Couchman H. M. P., Yoshida N., 2001, MNRAS, 321, 372
Keeton C. R., 1998, PhD thesis, Harvard University
Kaiser N., 1986, MNRAS, 222, 323
Kaiser N., 1992, ApJ, 388, 272
Kent S. M., 1985, ApJ, 59, 115
Kochanek C. S., White M., 2001, ApJ, 559, 531

Lacey C., Cole S., 1993, MNRAS, 262, 627

Lahav O., Rees M. J., Lilje P. B., Primack J. R., 1991, MNRAS, 251, 128

Li L., Ostriker P., 2000, preprint (astro-ph/0010432)

Łokas E. L., Hoffman Y., 2001, in Spooner N. J. C., Kudryavtsev V., eds, Proc. 3rd International Workshop on the Identification of Dark Matter. World Scientific, Singapore, p. 121

Macias-Perez J. F., Helbig P., Quast R., Wilkinson A., Davies R., 2000, A&A, 353, 419

Mandolesi N. et al., 1998, Low Frequency Instrument for Planck. A proposal to the European Space Agency

Mao S., Kochanek C. S., 1994, MNRAS, 268, 569

Maoz D., Rix H.-W., Gal-Yam A., Gould A., 1997, ApJ, 486, 75

Mellier Y., 1999, ARA&A, 37, 127

Mihalas D., Binney J., 1981, Galactic Astronomy. W. H. Freeman and Company, San Francisco 312

Miralda-Escudé J., 1991, ApJ, 380, 1

Monaco P., Salucci P., Danese L., 2000, MNRAS, 311, 279

Moore B., Quinn T., Governato F., Stadel J., Lake G., 1999, MNRAS, 310, 1147

Nakamura T. T., 1996, MSc thesis, Univ. Tokyo

Narayan R., White S. D. M., 1988, MNRAS, 231, 97

Narayan R., 1989, ApJ, 339, L53

Narayan R., 1998, New Astron. Rev., 42, 73

Narayan R., Bartelmann M., 1997, in Dekel A., Ostriker J. P., eds, Formation of Structure in the Universe. Cambridge University Press, Cambridge

Navarro J. F., Frenk C. S., White S. D. M., 1997, ApJ, 490, 493

Peacock J. A., 1982, MNRAS, 199, 987

Peebles P. J. E., 1980, The Large-Scale Structure of the Universe. Princeton Univ. Press, Princeton

Pei Y. C., 1995, ApJ, 440, 485

Porciani C., Madau P., 2000, ApJ, 532, 679

Press W. H., Schechter P., 1974, ApJ, 187, 425

Rix H.-W., Maoz D., Turner E. L., Fukugita M., 1994, ApJ, 435, 49

Saunders W., Rowan-Robinson M., Lawrence A., Efstathiou G., Kaiser N., Ellis R. S., Frenk C. S., 1990, MNRAS, 242, 318

Schneider P., 1992, A&A, 254, 14

Schneider P., Ehlers J., Falco E. E., 1992, Gravitational Lenses. Springer-Verlag, Heidelberg

Sheth R. K., Tormen G., 1999, MNRAS, 308, 119

Sheth R. K., Mo H. J., Tormen G., 2001, MNRAS, 323, 1

Silva L., Granato G. L., Bressan A., Danese L., 1998, ApJ, 509, 103

Smail I., Ivison R. J., Kneib J. P., Cowie L. L., Blain A. W., Barger A. J., Owen F. N., Morrison G. E., 1999, MNRAS, 308, 1061

Viana P., Liddle A. R., 1999, MNRAS, 303, 535

Vietri M., Ostriker J. P., 1983, ApJ, 267, 488

Wallington S., Narayan R., 1993, ApJ, 403, 517

Wright C. O., Brainerd T. G., 2000, ApJ, 534, 34

Wyithe J. S. B., Turner E. L., Spergel D. N., 2001, ApJ, 555, 504

This paper has been typeset from a TEX/LATEX file prepared by the author.